SAND2022-2298C

A New Rock Salt Constitutive Model with Back Stress and Drag Stress Hardening

Benjamin Reedlunn

Sandia National Laboratories, P.O. Box 5800, Albuquerque, NM 87112, USA

breedlu@sandia.gov

ABSTRACT: This paper presents a new, largely phenomenological, model for rock salt that includes branches for pressure solution and dislocation glide viscoplasticity. The dislocation glide branch utilizes back stress hardening for heterogeneously distributed dislocations and drag stress hardening for uniformly distributed dislocations. By transitioning between pressure solution at low strain rates, back stress dominated hardening at low to medium strain rates, and drag stress dominated hardening at high strain rates, a single model calibration can capture the behavior of Waste Isolation Pilot Plant salt over strain rates ranging from 10^{-12} to 10^{-4} 1/s, and temperatures from 20 to 60°C. The same model calibration can also predict the Bauschinger effect (and represent reverse creep). Although room for improvement exists, the model's elegant formulation can capture an assortment of damage-free behaviors.

1 Introduction

Rock salt constitutive models are used to simulate the evolution of mines, boreholes, storage caverns for gases and liquids, and nuclear waste repositories in rock salt formations. A wide variety of thermo-mechanical constitutive models have been proposed for rock salt, yet even the damage-free (micro-crack-free) thermoviscoplastic behavior remains difficult to capture. The Munson-Dawson model (Reedlunn et al. 2022), for example, can be calibrated against damage-free constant stress tests with low to medium steady-state strain rates (10^{-12} to 10^{-8} 1/s), but such a calibration fails to represent damage-free constant strain rate tests at high strain rates (10^{-6} to 10^{-4} 1/s). Capturing the damage-free behavior at these high strain rates is important because high strain rates are frequently used to characterize the mechanical behavior of damaged salt (dilated salt with micro-cracks). A constitutive model must first adequately capture damage-free behavior before attempting to represent how damage degrades salt's strength.

This paper presents a new model for the damage-free behavior of salt. Model development was influenced by a variety of models for metals (see J. Chaboche (2008) for a review) and the Aubertin, Yahya, et al. (1999) model for salt. Section 2 defines the new model formulation, Section 3 briefly discusses the formulation, Section 4 details four model calibrations, Section 5 partially validates the model, and Section 6 provides a short summary.

2 Model Formulation

Several preliminaries bear mentioning before defining the model formulation. First, compressive strains and stresses are treated as positive. Second, variables represented by capital letters are material constants, while variables represented by lower case letters are functions of other variables. Third, this section presents the model in an infinitesimal strain setting, but one can easily extended the model into the finite deformation realm using hypoelasticity.

The model additively decomposes the total strain rate $\dot{\varepsilon}$ into an elastic strain rate $\dot{\varepsilon}^{\text{el}}$, a thermal strain rate $\dot{\varepsilon}^{\text{th}}$, and a viscoplastic strain rate $\dot{\varepsilon}^{\text{vp}}$:

$$\dot{\varepsilon} = \dot{\varepsilon}^{\text{el}} + \dot{\varepsilon}^{\text{th}} + \dot{\varepsilon}^{\text{vp}}. \tag{1}$$

The elastic behavior utilizes generalized Hooke's law in rate form to relate $\dot{\varepsilon}^{\text{el}}$, the fourth-order isotropic elastic stiffness tensor $\mathbb{E}$, and the stress rate $\dot{\boldsymbol{\sigma}}$:

$$\dot{\boldsymbol{\sigma}} = \mathbb{E} : \dot{\varepsilon}^{\text{el}} = \mathbb{E} : \left(\dot{\varepsilon} - \dot{\varepsilon}^{\text{th}} - \dot{\varepsilon}^{\text{vp}}\right) \tag{2}$$

$$\mathbb{E} = (E_1 - \tfrac{2}{3} E_2)\, \boldsymbol{I} \otimes \boldsymbol{I} + 2\, E_2\, \mathbb{I}, \tag{3}$$

where E_1 is the bulk modulus, E_2 is the shear modulus, $\boldsymbol{I}$ is the second-order identity tensor, and $\mathbb{I}$ is the fourth-order symmetric identity tensor. The thermal strain portion of the model is simply

$$\dot{\varepsilon}^{\text{th}} = -A\, \dot{\theta}\, \boldsymbol{I} \tag{4}$$

where A is the coefficient of thermal expansion, and θ is the absolute temperature. The viscoplastic strain rate is additively decomposed into a pressure solution strain rate $\dot{\varepsilon}^{\text{ps}}$ and a dislocation glide strain rate $\dot{\varepsilon}^{\text{dg}}$

$$\dot{\varepsilon}^{\text{vp}} = \dot{\varepsilon}^{\text{ps}} + \dot{\varepsilon}^{\text{dg}}. \tag{5}$$

The $\dot{\varepsilon}^{\text{ps}}$ branch captures steady-state viscoplastic behavior at low stresses. This branch utilizes the following flow rule,

$$\dot{\varepsilon}^{\text{ps}} = \dot{\tilde{\varepsilon}}^{\text{ps}} \frac{\partial \tilde{\sigma}^{\text{ps}}}{\partial \boldsymbol{\sigma}}, \tag{6}$$

where $\dot{\tilde{\varepsilon}}^{\text{ps}}$ and $\tilde{\sigma}^{\text{ps}}$ are the equivalent pressure solution strain rate and stress, respectively. Pressure solution viscoplasticity is taken to be independent of the mean stress $\sigma^{\text{m}} = \text{tr}(\boldsymbol{\sigma})/3$ and driven entirely by the deviatoric stress $\boldsymbol{\sigma}^{\text{dev}}$, so the pressure solution stress is simply

$$\boldsymbol{\sigma}^{\text{ps}} = \boldsymbol{\sigma}^{\text{dev}} = \boldsymbol{\sigma} - \sigma^{\text{m}}\, \boldsymbol{I}. \tag{7}$$

This stress tensor is reduced to a scalar equivalent (von Mises) pressure solution stress as

$$\tilde{\sigma}^{\text{ps}} = \sqrt{\tfrac{3}{2}\, \boldsymbol{\sigma}^{\text{ps}} : \boldsymbol{\sigma}^{\text{ps}}}. \tag{8}$$

The equivalent pressure solution strain rate is given by

$$\dot{\tilde{\varepsilon}}^{\text{ps}} = P_1\, \exp\left(-\frac{P_2}{\theta}\right) \frac{\tilde{\sigma}^{\text{ps}}}{\theta}, \tag{9}$$

where P_j are material constants (C. Spiers et al. 1990). Eq. (9) assumes any non-zero $\tilde{\sigma}^{\text{ps}}$ causes pressure solution flow, such that the pressure solution quasi-static (rate-independent) yield surface is simply a point at $\boldsymbol{\sigma} = 0$.

The dislocation glide branch $\dot{\varepsilon}^{\text{dg}}$ dominates transient viscoplastic behavior at low stresses, and all viscoplastic behavior at medium to high stresses. Dislocation glide utilizes the following flow rule,

$$\dot{\varepsilon}^{\text{dg}} = \dot{\tilde{\varepsilon}}^{\text{dg}} \frac{\partial \tilde{\sigma}^{\text{dg}}}{\partial \boldsymbol{\sigma}}, \tag{10}$$

where $\dot{\tilde{\varepsilon}}^{\text{dg}}$ and $\tilde{\sigma}^{\text{dg}}$ are the equivalent dislocation glide strain rate and stress, respectively. In contrast to the pressure solution branch and the majority of other salt models, the model assumes dislocation glide is driven by a dislocation glide stress (a.k.a. effective stress)

$$\boldsymbol{\sigma}^{\text{dg}} = \boldsymbol{\sigma}^{\text{dev}} - \boldsymbol{b} \tag{11}$$

that includes $\boldsymbol{b}$, a second-order tensor called the back stress (a.k.a. internal stress). With this definition for $\boldsymbol{\sigma}^{\mathrm{dg}}$, the equivalent (von Mises) dislocation glide stress is

$$\tilde{\sigma}^{\mathrm{dg}} = \sqrt{\tfrac{3}{2}\,\boldsymbol{\sigma}^{\mathrm{dg}} : \boldsymbol{\sigma}^{\mathrm{dg}}}. \tag{12}$$

Unlike the pressure solution branch, the dislocation glide branch has a finite size, quasi-static, yield surface, defined as

$$g = \tilde{\sigma}^{\mathrm{dg}} - G_0\, y, \tag{13}$$

where G_0 is a material constant and y is an isotropic hardening variable called the drag stress that evolves from a positive initial value Y_0 to some positive value. By default, $G_0 = E_2 \times 10^{-10}/Y_0$, which makes the $g = 0$ surface typically very small relative to $\tilde{\sigma}^{\mathrm{dg}}$. The equivalent dislocation glide strain rate is

$$\dot{\tilde{\varepsilon}}^{\mathrm{dg}} = \begin{cases} 0 & \text{for } g < 0 \\ G_1\, \exp\left(-\dfrac{G_2}{\theta}\right) \left[\sinh\left(\dfrac{\tilde{\sigma}^{\mathrm{dg}}}{y}\right)\right]^{G_3} & \text{for } g \geq 0 \end{cases}, \tag{14}$$

where G_j are material constants. The $g \geq 0$ expression applies for both transient and steady-state creep, but it is motivated by the Garofalo (1963) steady-state creep expression.

The drag stress y evolves according to the following differential equation,

$$\dot{y} = Y_1 \left(\frac{Y_1}{y}\right)^{Y_2} \left(1 - \frac{y}{\bar{y}}\right) \dot{\tilde{\varepsilon}}^{\mathrm{dg}}, \tag{15}$$

where

$$\bar{y} = \frac{\bar{\sigma} - \bar{b}}{\sinh^{-1}\left\{\left[\dfrac{\dot{\tilde{\varepsilon}}^{\mathrm{dg}}}{G_1\, \exp\left(-G_2/\theta\right)}\right]^{1/G_3}\right\}} \tag{16}$$

is the drag stress saturation ($\bar{y} \geq Y_0$),

$$\bar{\sigma} = Y_4\, \sinh^{-1}\left\{\left[\frac{\dot{\tilde{\varepsilon}}^{\mathrm{dg}}}{Y_3\, \exp\left(-G_2/\theta\right)}\right]^{1/Y_5}\right\} \tag{17}$$

is the equivalent (von Mises) stress saturation, $\bar{b}$ is the equivalent back stress saturation (discussed below), and Y_j are material parameters.

The back stress has a similar, yet different, set of evolution equations. Following J.-L. Chaboche (1986), $\boldsymbol{b}$ is decomposed as

$$\boldsymbol{b} = \sum_{j=1}^{2} \boldsymbol{b}_j, \tag{18}$$

where $\boldsymbol{b}_1$ is a short range, quickly evolving, back stress and $\boldsymbol{b}_2$ is a long range, slowly evolving, back stress. Each back stress has an equivalent back stress defined as

$$\tilde{b}_j = \sqrt{\frac{3}{2}\,\boldsymbol{b}_j : \boldsymbol{b}_j}. \tag{19}$$

Each back stress begins at $\boldsymbol{B}_{j0}$, which must be deviatoric ($\mathrm{tr}(\boldsymbol{B}_{j0}) = 0$) and is set to the zero tensor $\mathbf{0}$ by default. As deformation proceeds, each back stress evolves according to

$$\dot{\boldsymbol{b}}_j = B_{j1}\left(\frac{2}{3}\,\dot{\varepsilon}^{\,\mathrm{dg}} - \frac{\boldsymbol{b}_j}{\bar{b}_j}\,\dot{\tilde{\varepsilon}}^{\,\mathrm{dg}}\right), \tag{20}$$

where

$$\bar{b}_j = B_{j2}\,B_{j3}\,\tanh\left(\frac{\bar{\sigma}}{B_{j3}}\right) \tag{21}$$

is the j^{th} equivalent back stress saturation and B_{jk} are material constants. Analogous to Eq. (18), the equivalent back stresses can be summed as

$$\tilde{b} = \sum_{j=1}^{2} \tilde{b}_j \qquad \text{and} \qquad \bar{b} = \sum_{j=1}^{2} \bar{b}_j. \tag{22}$$

All materials parameters should be non-negative to obtain typical material behavior. Furthermore, $1 - \sum_{j=1}^{2} B_{j2}$ must be non-negative to ensure $\bar{\sigma} - \bar{b}$ in Eq. (16) is positive.

3 Discussion of Model Formulation

This section briefly discusses some salient details of the model formulation. A more thorough discussion will be published at a later date.

3.1 Lack of Coupling Between Branches

The model assumes that $\dot{\varepsilon}^{\,\mathrm{ps}}$ and $\dot{\varepsilon}^{\,\mathrm{dg}}$ are largely independent processes because pressure solution occurs along the grain boundaries, while dislocation glide occurs inside the grains. One potential mode of coupling, however, has been experimentally observed for $\theta \geq 75$ °C: recrystallization by brine-assisted grain boundary migration (Ter Heege et al. 2005). This process consumes grains with high dislocation density, changes the average grain size, and requires significant strain ($\tilde{\varepsilon}^{\,\mathrm{vp}} > 10$ %) to be activated. A reduction in dislocation-based hardening could be implicitly captured by calibrating the model against laboratory experiments that include recrystallization, but the model does not attempt to capture the impact of grain size changes on pressure solution viscoplasticity. Omitting this coupling is likely insignificant in many applications since $\tilde{\varepsilon}^{\,\mathrm{vp}} > 10$ % tends to occur close to drifts and caverns, where pressure solution creep is not the dominant mechanism.

3.2 Pressure Solution Branch

The pressure solution branch consists solely of steady-state deformation, without any hardening (transient strain), for several reasons. According to classical pressure solution theory, the increase in salt solubility in a brine film, of 0.1 μm thickness, surrounding a grain, of 10 mm size, due to a 1 MPa increase in $\tilde{\sigma}^{\,\mathrm{ps}}$, at $\theta = 100$ °C would produce a negligible transient creep strain on the order of 10^{-8} (C. J. Spiers 2021). Non-classical effects, such as pressure solution-based redistribution of grain boundary stresses, grain coarsening, grain elongation, or other structural changes to grain boundaries, could perhaps create a hardening effect, but a succinct, quantitative, description of such effects is not known to the author. On the other hand, the existence of sub-grains corresponding to low stresses in in-situ deformed samples (Carter et al. 1993) and reverse creep at low stresses (Gharbi et al. 2020) suggest that dislocation glide is active during

low stress creep, even if dislocation glide does not dominate the steady-state rate. It, therefore, seems reasonable to assume dislocation glide creep dominates transient creep at low stresses, while pressure solution creep dominates steady-state creep at low stresses.

3.3 Dislocation Glide Branch

Although the dislocation glide branch is largely phenomenological, some loose physical meaning can be attached to the back stresses and drag stress. The back stresses represent hardening due to heterogenously distributed dislocation substructures, such as sub-grains and wavy slip bands produced by dislocation climb and cross-slip, respectively (Carter et al. 1993). These substructures are commonly observed at low to medium strain rates ($10^{-12} \leq \dot{\tilde{\varepsilon}}^{\mathrm{vp}} \leq 10^{-8}$ 1/s) and low to high temperatures ($20 \leq \theta \leq 700\,^{\circ}$C). The drag stress represents hardening due to more uniform dislocation distributions, as are observed at higher strain rates (Raj et al. 1989).

The motivation behind the name "drag stress" can be seen by inverting the $g \geq 0$ case in Eq. (14) as

$$\tilde{\sigma}^{\mathrm{dg}} = y \, \sinh^{-1}\left\{\left[\frac{\dot{\tilde{\varepsilon}}^{\mathrm{dg}}}{G_1 \, \exp\left(-G_2/\theta\right)}\right]^{1/G_3}\right\}, \tag{23}$$

in which $\tilde{\sigma}^{\mathrm{dg}}$ is equal to y multiplied by a non-linear function of $\dot{\tilde{\varepsilon}}^{\mathrm{dg}}$. Thus, y plays a role similar to an evolving dashpot in rheological models.

Another important observation is the stresses $\boldsymbol{\sigma}^{\mathrm{dg}}$, and $\boldsymbol{b}$ are co-axial along proportional stress paths, such that Eqs. (11) and (12) can be simplified to

$$\tilde{\sigma} = \tilde{b} + \tilde{\sigma}^{\mathrm{dg}}, \tag{24}$$

where $\tilde{\sigma} = \sqrt{\frac{3}{2}\,\boldsymbol{\sigma}^{\mathrm{dev}} : \boldsymbol{\sigma}^{\mathrm{dev}}}$. Eq. (24) can be seen as decomposing $\tilde{\sigma}$ into a back stress contribution $\tilde{b}$ and a drag stress contribution $\tilde{\sigma}^{\mathrm{dg}}$ (see Eq. (23)) when $\dot{\tilde{\varepsilon}}^{\mathrm{dg}}$ is controlled, as approximately occurs in a constant strain rate test.

Both hardening evolution equations (Eqs. (15) and (20)) conform to the Bailey-Orowan concept, in which the hardening rate is the result of a competition between a strain hardening term and a strain (a.k.a. dynamic) recovery term. Hardening saturates when the hardening and recovery rates balance one another ($\dot{y} = 0$ and $\dot{\boldsymbol{b}}_j = \boldsymbol{0}$). At hardening saturation, $\tilde{b}_j = \bar{b}_j$, $y = \bar{y}$, the stresses $\boldsymbol{\sigma}^{\mathrm{dg}}$ and $\boldsymbol{b}$ are co-axial (even for non-proportional stress paths), such that Eqs. (14), (16), (17) and (24) combine to give $\tilde{\sigma} = \bar{\sigma}$. Inverting the expression for $\bar{\sigma}$ in Eq. (17) results in the Garofalo (1963) steady-state dislocation glide strain rate expression:

$$\dot{\tilde{\varepsilon}}^{\mathrm{dg}} = Y_3 \, \exp\left(-\frac{G_2}{\theta}\right)\left[\sinh\left(\frac{\bar{\sigma}}{Y_4}\right)\right]^{Y_5}. \tag{25}$$

One can rearrange Eq. (16) into a form similar to Eq. (24) as

$$\bar{\sigma} = \bar{b} + \bar{\sigma}^{\mathrm{dg}}, \tag{26}$$

which shows that one must decide how to partition the hardening saturation between back stress and drag stress contributions. The hyperbolic tangent in Eq. (21) assumes back stress contributions dominate at low stresses (low strain rates) and drag stress contributions dominate at high stresses (high strain rates). This critical premise is based on direct measurements of the back stress in single phase metals (Takeuchi et al. 1976, Figure 15), the microstructural observations at the start of this sub-section, and the study discussed in Section 5.

4 Calibration

This section reviews four model calibrations against damage-free axisymmetric compression tests on salt from the Waste Isolation Pilot Plant (WIPP). Attention is focused on calibration performance rather than the calibration procedure.

Many details of the axisymmetric compression tests on WIPP salt can be found in Salzer et al. (2015), Düsterloh et al. (2015), and Reedlunn et al. (2022), but some points are reviewed herein. The specimen grain sizes ranged from 2 to 28 mm, with an arithmetic average of 10 mm. Each test began with a hydrostatic consolidation stage for one to ten days at 20 MPa of pressure. The logarithmic axial strain and logarithmic inelastic volumetric strains at the end of the consolidation stage are denoted as $\varepsilon_{zz}(t_0)$ and $\varepsilon^{ie}_{vol}(t_0)$, respectively, while $\varepsilon_{zz} - \varepsilon_{zz}(t_0)$ and $\varepsilon^{ie}_{vol} - \varepsilon^{ie}_{vol}(t_0)$ are the strain changes thereafter. Each constant stress test involved two non-zero $\bar{\sigma}$ stages. The first creep stage was designed to approach the steady-state strain rate from "above", while the second creep stage was meant to approach the steady-state strain rate from "below", as discussed in Günther et al. (2015). In the constant strain rate tests, the axial engineering strain rate $\dot{e}_{zz}$ was held fixed, not the axial logarithmic strain rate $\dot{\varepsilon}_{zz} = \dot{e}_{zz}/(1 - e_{zz})$, so care was taken to convert between the two strain rate measures as needed. After the consolidation stage, the radial confining pressure was held at σ_{rr} = 10 or 20 MPa to avoid significant micro-cracking. Despite these confining pressures, some samples still developed significant micro-cracks towards the end of the test, judging by $\varepsilon^{ie}_{vol} - \varepsilon^{ie}_{vol}(t_0)$. Consequently, only stress–strain curve segments corresponding to $\varepsilon^{ie}_{vol} - \varepsilon^{ie}_{vol}(t_0) \geq 0$ (compressive inelastic volume strain) were treated as micro-crack-free and suitable for model calibration. One exception to this rule was made to compute the saturation stress $\bar{\sigma}$ from test A_TUC_TC98, as noted below.

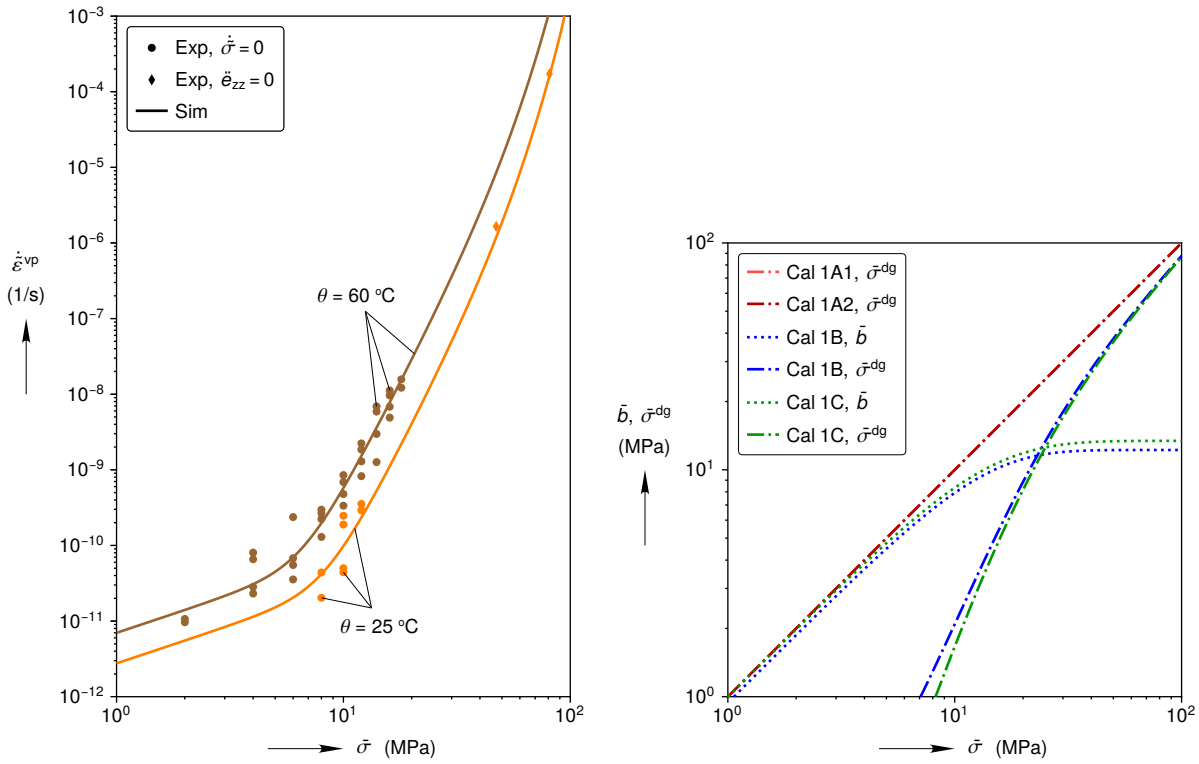

(a) Model fit to steady-state strain rate measurements

(b) Back stress and drag stress contributions (the Cal 1A1 and 1A2 $\bar{\sigma}^{dg}$ curves overlap)

Figure 1: Model behavior at hardening saturation (steady-state).

The experimental measurements in Fig. 1a were derived from measuring the steady-state strain rate in constant stress experiments and the saturation stress in two constant strain rate experiments, all with σ_{rr} = 20 MPa. In the faster constant strain rate test, A_TUC_TC98, the maximum stress of 75.2 MPa corresponded to $\varepsilon_{zz} - \varepsilon_{zz}(t_0)$ = 42.2 % and $\varepsilon_{vol}^{ie} - \varepsilon_{vol}^{ie}(t_0)$ = –0.8 %. As micro-cracking likely affected this maximum stress, the stress–strain slope at the onset of expansion ($\varepsilon_{vol}^{ie} - \varepsilon_{vol}^{ie}(t_0) < 0$) was linearly extended to $\varepsilon_{zz} - \varepsilon_{zz}(t_0)$ = 42.2 %, resulting in 86.8 MPa, and a micro-crack-free saturation stress was roughly estimated as $\bar{\sigma}$ = (75.2 + 86.8)/2 = 81.0 MPa. The logarithmic scale in Fig. 1a makes a 75.2 to 86.8 MPa uncertainty virtually negligible, so 81.0 MPa was treated as a reliable data point.

Several calibration decisions were made in the absence of specific recent experimental measurements on WIPP salt. (1) The thermoelastic parameters in Table 1 were inherited from Munson et al. (1989). (2) The parameter G_1 was set to 10^9 1/s. (3) The initial drag stress was set to Y_0 = 1.0 MPa, since preliminary simulations showed the model's response was insensitive to Y_0 when $\tilde{\sigma} > 2\,Y_0$. (4) Back stress hardening prior to testing was neglected ($\boldsymbol{B}_{j0} = \boldsymbol{0}$). (5) The parameter P_2 was set to 2950 K, based on the granular salt compaction experiments in C. Spiers et al. (1990). (6) The calibrations focused on the $20 \le \theta \le 60\,^{\circ}$C temperature range.

With the parameters G_1 and P_2 selected, the strain rate saturation parameters P_1, G_2, Y_3, Y_4, and Y_5 were optimized, in a least squares sense, against the steady-state strain rate measurements. The resulting fits are shown in Fig. 1a and the parameter values are listed in Table 1. All four model calibrations utilize the same steady-state strain rate calibration.

The hardening parameters were fit against the strain vs. time curves from the first stage of the constant stress tests and the stress vs. strain curves from the damage-free portions of the constant strain rate tests. The fitting process minimized a merit function that compared simulations against experimental measurements in an integrated least-squares sense. The resulting parameter sets are listed in Table 1. The performance of each hardening calibration is shown in Figs. 2 and 3. Figure 2a depicts the transient creep strain $\tilde{\varepsilon}^{tr}(t_1)$ after $t_1 \approx 50$ days of creep at various applied stresses and two temperatures. (The transient strain $\tilde{\varepsilon}^{tr} = \tilde{\varepsilon}^{tr}(t)$ is ε_{zz} minus the elastic and accumulated steady-state creep strain.) Fig. 2b depicts the characteristic creep time t^{ch}, which is the time for $\tilde{\varepsilon}^{tr}$ to reach $0.8\,\tilde{\varepsilon}^{tr}(t_1)$. Each simulated curve, for a given temperature, in Fig. 2 was derived from one hundred individual constant stress simulations. Each constant stress simulation utilized a different $\bar{\sigma}$, ranging from 1 to 100 MPa. Values of $\tilde{\varepsilon}^{tr}(t_1)$ and t^{ch} were extracted from each simulated strain history in the same manner as the experiments. Note that salt tends to approach steady-state creep in less time when tested at higher temperatures and stresses than at lower temperatures and stresses, so, by focusing on a fixed time, Fig. 2 plots the transient behavior at various degrees of proximity to true steady-state creep. Although one should be cautious about comparing the transient behavior at different stresses and temperatures in Fig. 2, one can still directly compare experimental measurements and simulations at a given stress and temperature. Finally, the plots in Fig. 3 show the stress vs. strain curves for constant strain rate experiments and simulations at three different engineering strain rates. Only the $\varepsilon_{vol}^{ie} - \varepsilon_{vol}^{ie}(t_0) \ge 0$ portions of the experimental measurements are shown, which is why some measured responses abruptly terminate.

Calibration 1A1 optimized G_3, Y_1, and Y_2 against the first-stage constant stress tests with $10 \le \tilde{\sigma} \le 18$ MPa. The Calibration 1A1 simulations of constant stress tests produce $\tilde{\varepsilon}^{tr}(t_1)$ and t^{ch} values that agree with the experimental measurements (see Figs. 2a and 2b) within the calibration range, but not outside the calibration range. The constant stress simulations at $\tilde{\sigma} \le 6$ MPa under-predict the $\tilde{\varepsilon}^{tr}(t_1)$ values (see Fig. 2a), and the constant strain rate simulations substantially under-predict the stresses for $\varepsilon_{zz} - \varepsilon_{zz}(t_0) > 1$ % at all three strain rates (see Fig. 3a). This latter under-prediction is especially problematic because a model that cannot

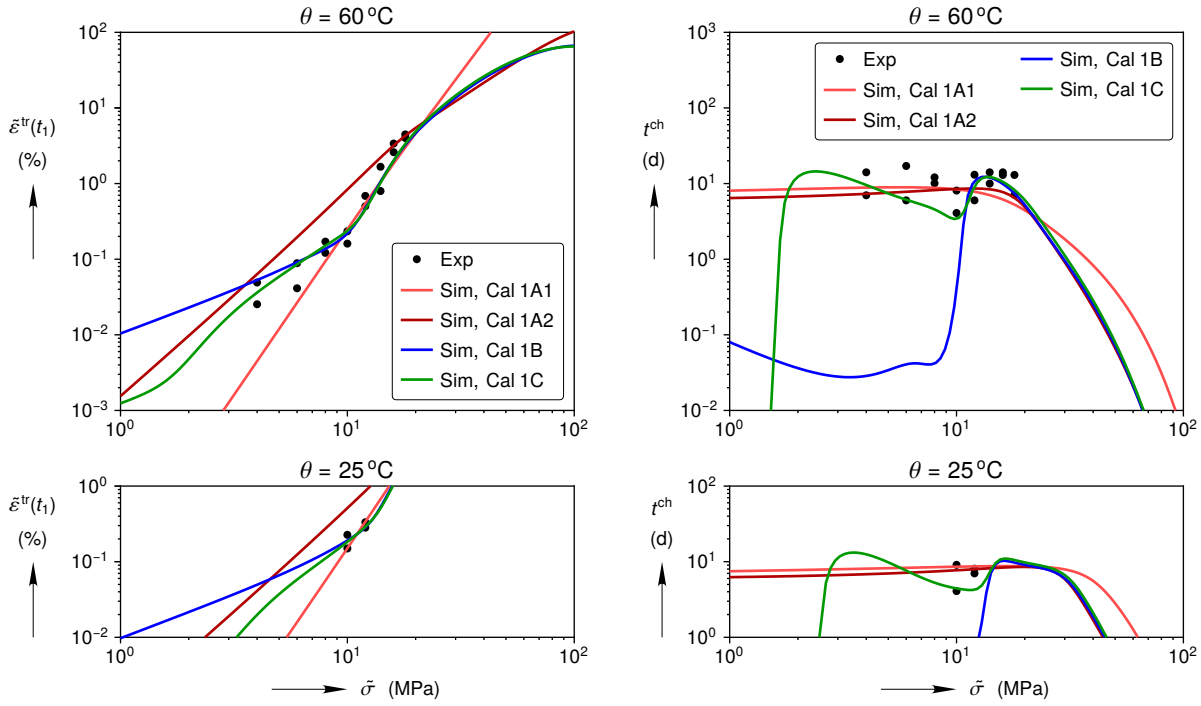

(a) Transient creep strain at $t_1 \approx 50$ d

(b) Characteristic creep time

Figure 2: Transient strains and characteristic times from constant stress simulations compared against experimental measurements (first constant stress stage only).

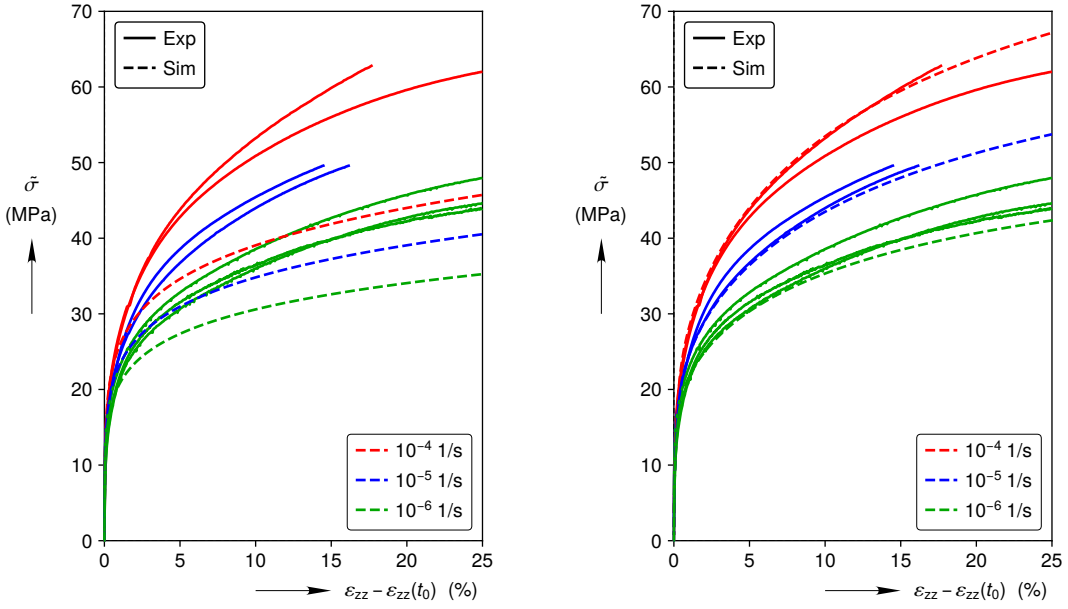

(a) Calibration 1A1

(b) Calibration 1C

Figure 3: Stress–strain curves from room temperature constant strain rate simulations from Calibration 1A1 and 1C compared against experimental measurements. (Constant strain rate simulation results for Calibrations 1A2 and 1B were similar to the Calibration 1C results in (b).)

capture damage-free constant strain rate behavior cannot be used to infer the degree of damage in low confining pressure constant strain rate tests.

Calibration 1A2, by contrast, optimized G_3, Y_1, and Y_2 against the constant strain rate tests with $10^{-6} \leq \dot{e}_{zz} \leq 10^{-4}$ 1/s. The back stress evolution rates were again set to zero ($B_{j1} = 0$). The Calibration 1A2 simulations produced stress–strain responses similar to the Calibration 1C responses shown in Fig. 3b as desired, but simulations of the constant stress tests at $\tilde{\sigma} <$ 16 MPa substantially over-predicted $\tilde{\varepsilon}^{\text{tr}}(t_1)$ (see Fig. 2a).

Calibration 1B fit G_3, Y_1, Y_2, B_{21}, B_{22}, and B_{23} against the first-stage constant stress tests with $10 \leq \tilde{\sigma} \leq 18$ MPa and the constant strain rate tests with $10^{-6} \leq \dot{e}_{zz} \leq 10^{-4}$ 1/s. The short range back stress evolution rate was set to zero ($B_{11} = 0$). Calibration 1B captured the measured $\tilde{\varepsilon}^{\text{tr}}(t_1)$ and t^{ch} values for $10 \leq \tilde{\sigma} \leq 18$ MPa (see Figs. 2a and 2b), and the Calibration 1B stress-strain curves were similar to the Calibration 1C curves (see Fig. 3b). Outside of the calibration range, Calibration 1B reasonably predicted the $\tilde{\varepsilon}^{\text{tr}}(t_1)$ values for $4 \leq \tilde{\sigma} \leq 8$ MPa, but under-predicted the t^{ch} measurements by roughly 100× in the same stress range.

Calibration 1C fit G_3, Y_1, Y_2, B_{11}, B_{13}, B_{21}, B_{22}, and B_{23} against the first-stage constant stress tests with $4 \leq \tilde{\sigma} \leq 18$ MPa and the constant strain rate tests with $10^{-6} \leq \dot{e}_{zz} \leq 10^{-4}$ 1/s. Preliminary optimizations that allowed both B_{12} and B_{22} to vary produced $B_{12} + B_{22} \approx 0.999$ (recall $B_{12}+B_{22} > 1$ is prohibited), so $B_{12} = 1-B_{22}$ was simply enforced for the final Calibration 1C optimization. This most flexible model calibration produced behaviors similar to Calibration 1B, except it more accurately captured the t^{ch} measurements at $4 \leq \tilde{\sigma} \leq 8$ MPa (see Fig. 2b).

The relative contributions of the back stresses and drag stress at hardening saturation can be seen in Fig. 1b for each of the calibrations. Calibrations 1A1 and 1A2 do not include back stresses, so the drag stress contribution $\bar{\sigma}^{\text{dg}}$ dominates at all applied stresses and strain rates. Calibrations 1B and 1C, however, conform to the assumption discussed at the end of Section 3.3: $\bar{b}$ dominates at low stresses and $\bar{\sigma}^{\text{dg}}$ dominates at high stresses.

Table 1: Calibrations (All calibrations utilize the default values of $G_0 = E_2 \times 10^{-10}/Y_0$ and $\boldsymbol{B}_{j0} = \boldsymbol{0}$.)

Type	Parameter	Units	Cal 1A1	Cal 1A2	Cal 1B	Cal 1C
Thermo-elastic	E_1	Pa	20.67×10^9	20.67×10^9	20.67×10^9	20.67×10^9
	E_2	Pa	12.40×10^9	12.40×10^9	12.40×10^9	12.40×10^9
	A	1/K	45×10^{-6}	45×10^{-6}	45×10^{-6}	45×10^{-6}
Pressure Solution	P_1	K/(Pa s)	16.39×10^{-12}	16.39×10^{-12}	16.39×10^{-12}	16.39×10^{-12}
	P_2	K	2.950×10^3	2.950×10^3	2.950×10^3	2.950×10^3
Dislocation Glide	G_1	1/s	1×10^9	1×10^9	1×10^9	1×10^9
	G_2	K	5.585×10^3	5.585×10^3	5.585×10^3	5.585×10^3
	G_3	–	22.03	14.12	8.543	7.973
	Y_0	Pa	1×10^6	1×10^6	1×10^6	1×10^6
	Y_1	Pa	86.08×10^6	221.6×10^6	451.6×10^6	496.7×10^6
	Y_2	–	4.240	2.138	1.035	0.9911
	Y_3	1/s	36.00	36.00	36.00	36.00
	Y_4	Pa	43.50×10^6	43.50×10^6	43.50×10^6	43.50×10^6
	Y_5	–	5.623	5.623	5.623	5.623
	B_{11}	Pa	0	0	0	84.63×10^9
	B_{12}	–	1×10^{-9}	1×10^{-9}	1×10^{-9}	0.2910
	B_{13}	Pa	1×10^9	1×10^9	1×10^9	18.60×10^6
	B_{21}	Pa	0	0	8.303×10^9	5.445×10^9
	B_{22}	–	1×10^{-9}	1×10^{-9}	0.9420	0.7090
	B_{23}	Pa	1×10^9	1×10^9	12.98×10^6	11.29×10^6

5 Partial Validation

The previous section demonstrated how the drag stress and two back stresses can be used to capture salt's damage-free behavior at different stresses and strain rates. All the calibration experiments, however, involved monotonic proportional stress paths. This section compares model calibrations 1A2, 1B, and 1C against a constant strain rate experiment with a non-monotonic proportional stress path. Such loading direction reversals lead to a temporary reduction in flow strength known as the Bauschinger effect. This effect is frequently attributed to microstructural residual stresses associated with heterogenous dislocation distributions, such as sub-grains (see Mughrabi (1983, Fig. 4)).

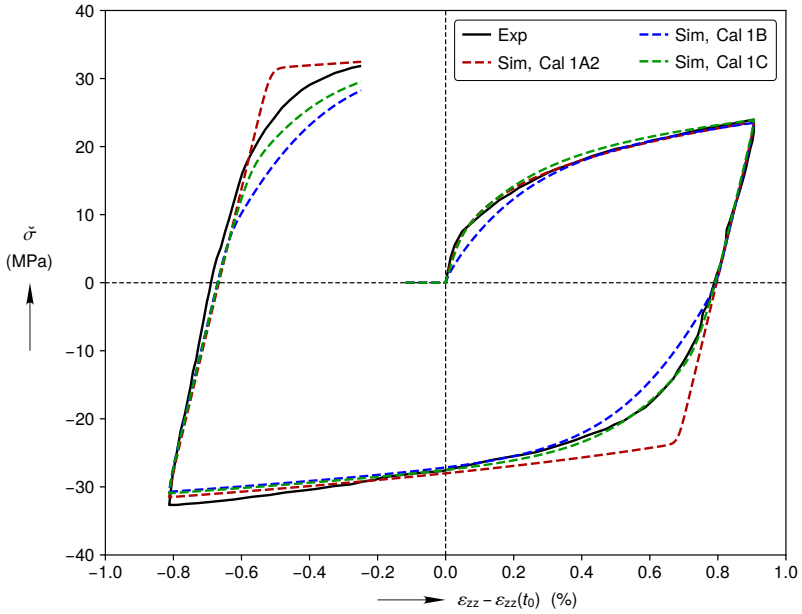

Figure 4: A comparison of three different model calibration stress–strain responses against experimental measurements on artificial rock salt.

The Bauschinger effect has not been studied on WIPP salt, so an experiment on artificial rock salt (Aubertin, Julien, et al. 1999, Fig. 5d) was utilized instead. Fig. 4 displays the artificial rock salt stress–strain response at $|\dot{\varepsilon}_{zz}| = 3.5 \times 10^{-5}$ 1/s, $\sigma_{rr} = 53$ MPa, and $\theta = 20$ °C, during three stages: axisymmetric compression, axisymmetric extension, and a second axisymmetric compression stage*. This artificial rock salt experiment was simulated using slightly modified versions of Calibration 1A2, 1B, and 1C. The elastic moduli E_1 and E_2 were both reduced by a factor of 22.5/31.0 = 0.7258 to properly capture the artificial rock salt's linear elastic behavior, as reported by Aubertin, Yahya, et al. (1999). In addition, the simulated stress difference $\breve{\sigma} = \sigma_{zz} - \sigma_{rr}$ values were scaled by 0.92× to bring the WIPP salt derived predictions more in-line with the artificial salt measurements during the first axisymmetric compression stage.

Fig. 4 also compares the simulated stress–strain responses against the experimental measurements. The (scaled) $\breve{\sigma}$ from Calibration 1A2, which includes only drag stress hardening, matches the experimental measurements nearly exactly during the first axisymmetric compression stage, but fails to capture the Bauschinger effect during the axisymmetric extension and

*To enhance legibility, brief elastic unloading and reloading stages in the actual experiment were omitted, and the measured stress and strain were each multiplied by –1 to cause the first stage to be axisymmetric compression rather than axisymmetric extension.

second axisymmetric compression stages. Adding one back stress in Calibration 1B produces a prediction that qualitatively represents the Bauschinger effect, but the prediction is not quite stiff enough at the onset of hardening and re-hardening. Adding a second kinematic hardening back stress causes Calibration 1C to accurately represent the initial hardening during the first axisymmetric compression stage, accurately *predict* the re-hardening during the axisymmetric extension stage, and come closer to predicting the re-hardening during the second axisymmetric compression stage.

This prediction of the Bauschinger effect is significant because the Calibration 1C back stress was not calibrated against tests with non-monotonic loading, as is often done. Instead, the back stress parameters B_{ij} were calibrated against monotonic loading tests, such that the back stress dominated at low strain rates (low stresses) and played a lesser, yet significant, role at high strain rates (high stresses) (see Fig. 1b). The successful prediction of the Bauschinger effect by Calibration 1C, therefore, validates the hyperbolic tangent in Eq. (21).

Although not shown herein, the model can also represent reverse creep during a multi-stage constant stress experiment. During forward creep at an applied $\tilde{\sigma}$, $\tilde{b}$ evolves to some value $\tilde{b} < \tilde{\sigma}$. Subsequently decreasing $\tilde{\sigma}$ to $\tilde{\sigma} < \tilde{b}$ produces reverse creep (see Eq. (10)).

6 Summary

A new model for the thermo-viscoplastic behavior of damage-free rock salt has been developed, calibrated, and partially validated. The pressure solution branch captured salt's steady-state behavior at low stresses. The dislocation glide branch captured WIPP salt's transient behavior at low stresses, and all observed viscoplastic behavior at medium to high stresses. After calibrating the model against monotonic experiments, the model successfully predicted the Bauschinger effect in a non-monotonic experiment. This result validates a key assumption in the model: the back stress dominates at low strain rates (low stresses) and the drag stress dominates at high strain rates (high stresses). Future work will likely focus on adding damage and healing to the model.

Acknowledgements

The author gratefully acknowledges the assistance of his Sandia colleagues, his Joint Project WEIMOS colleagues, and Christopher Spiers. Sandia National Laboratories is a multi-mission laboratory managed and operated by National Technology and Engineering Solutions of Sandia, LLC., a wholly owned subsidiary of Honeywell International, Inc., for the U.S. Department of Energy's National Nuclear Security Administration under contract DE-NA0003525. This research is funded by WIPP programs administered by the Office of Environmental Management (EM) of the U.S. Department of Energy. This paper describes objective technical results and analysis. Any subjective views or opinions that might be expressed in the paper do not necessarily represent the views of the U.S. Department of Energy or the United States Government.

References

Aubertin, M., Julien, M. R., Servant, S., and Gill, D. E. (1999). A rate-dependent model for the ductile behavior of salt rocks. Canadian Geotechnical Journal, 36, 4, 660–674.

Aubertin, M., Yahya, O. M. L., and Julien, M. (1999). Modeling mixed hardening of alkali halides with a modified version of an internal state variables model. International Journal of Plasticity, 15, 10, 1067–1088.

Carter, N., Horseman, S., Russell, J., and Handin, J. (1993). Rheology of rocksalt. Journal of Structural Geology, 15, 9-10, 1257–1271.

Chaboche, J.-L. (1986). Time-independent constitutive theories for cyclic plasticity. International Journal of plasticity, 2, 2, 149–188.

Chaboche, J. (2008). A review of some plasticity and viscoplasticity constitutive theories. International Journal of Plasticity, 24, 10, 1642–1693.

Düsterloh, U., Herchen, K., Lux, K.-H., Salzer, K., Günther, R.-M., Minkley, W., Hampel, A., Argüello Jr, J. G., and Hansen, F. D. (2015). Joint Project III on the comparison of constitutive models for the thermomechanical behavior of rock salt. III. Extensive laboratory test program with argillaceous salt from WIPP and comparison of test results. Proc. 8th Conference on the Mechanical Behavior of Salt, 13–21.

Garofalo, F. (1963). An empirical relation defining the stress dependence of minimum creep rate in metals. Trans. AIME, 227, 351–356.

Gharbi, H., Bérest, P., Blanco-Martín, L., and Brouard, B. (Oct. 2020). Determining upper and lower bounds for steady state strain rate during a creep test on a salt sample. International Journal of Rock Mechanics and Mining Sciences, 134, 104452.

Günther, R.-M., Salzer, K., Popp, T., and Lüdeling, C. (2015). Steady-state creep of rock salt: improved approaches for lab determination and modelling. Rock Mechanics and Rock Engineering, 48, 6, 2603–2613.

Mughrabi, H. (1983). Dislocation wall and cell structures and long-range internal stresses in deformed metal crystals. Acta metallurgica, 31, 9, 1367–1379.

Munson, D. E., Fossum, A. F., and Senseny, P. E. (1989). Advances in resolution of discrepancies between predicted and measured in situ WIPP room closures. Tech. rep. SAND88-2948, Albuquerque, NM, USA: Sandia National Laboratories.

Raj, S. V. and Pharr, G. (1989). Creep substructure formation in sodium chloride single crystals in the power law and exponential creep regimes. Materials Science and Engineering: A, 122, 2, 233–242.

Reedlunn, B., Argüello, J. G., and Hansen, F. D. (2022). A Reinvestigation into Munson's Model for Room Closure in Bedded Rock Salt. International Journal of Rock Mechanics and Mining Sciences, 151, doi: 10.1016/j.ijrmms.2021.105007.

Salzer, K., Günther, R.-M., Minkley, W., Naumann, D., Popp, T., Hampel, A., Lux, K.-H., Herchen, K., Düsterloh, U., Argüello Jr, J. G., and Hansen, F. D. (2015). Joint Project III on the comparison of constitutive models for the thermomechanical behavior of rock salt. II. Extensive laboratory test program with clean salt from WIPP. Proc. 8th Conference on the Mechanical Behavior of Salt, 3–12.

Spiers, C. J. (2021). Negligible transient strain due to pressure solution. Personal Communication.

Spiers, C., Schutjens, P., Brzesowsky, R., Peach, C., Liezenberg, J., and Zwart, H. (1990). Experimental determination of constitutive parameters governing creep of rocksalt by pressure solution. Geological Society, London, Special Publications, 54, 1, 215–227.

Takeuchi, S. and Argon, A. (1976). Steady-state creep of single-phase crystalline matter at high temperature. Journal of Materials Science, 11, 8, 1542–1566.

Ter Heege, J., De Bresser, J., and Spiers, C. (2005). Dynamic recrystallization of wet synthetic polycrystalline halite: dependence of grain size distribution on flow stress, temperature and strain. Tectonophysics, 396, 1-2, 35–57.